Research Article | Vol. 29, No. 23 / 8 Nov 2021 / Optics Express 38140
Optics EXPRESS

Attosecond-precision balanced linear-optics timing detector

TONG WANG,[1] QUN REN,[1] KEMAL ŞAFAK,[2] FRANZ X. KÄRTNER,[3,5] AND MING XIN[1,4,6]

[1]School of Electrical and Information Engineering, Tianjin University, Tianjin, 300072, China
[2]Cycle GmbH, Notkestraße 85, 22607 Hamburg, Germany
[3]Center for Free-Electron Laser Science, DESY and Hamburg University, Notkestraße 85, 22607 Hamburg, Germany
[4]Tianjin Key Laboratory of Brain-Inspired Intelligence Technology, Tianjin, 300072, China
[5]franz.kaertner@cfel.de
[6]xinm@tju.edu.cn

Abstract: A new timing detection method based on acousto-optic modulation is demonstrated. The timing detector is immune to dispersion effects and the environmental and laser amplitude noise can be well suppressed by a balanced configuration. With 1 mW power per pulse train, the measured timing noise floor is about 1×10^{-10} fs^2/Hz, which is close to the shot noise limit. The integrated timing jitter is 26 as at [1 Hz, 1 MHz]. With 170 fs pulse width and typical detector parameters, the calculated detector's timing noise floor is more than 5 and 12 orders of magnitude lower than that of a BOC, at 1 mW and 1 μW input power, respectively. This timing detector has a variety of potential applications in ultra-long fiber link stabilization, quantum metrology, weak signal timing control, etc.

1. Introduction

High-precision timing detectors are regarded as key components in numerous frontier applications. For instance, in the next-generation photon-science instruments such as X-ray free-electron lasers (XFELs) [1–3], effective timing detection is necessary for timing distribution with fiber links [4], remote laser/microwave synchronization [5–7] and pump-probe measurements [8,9] to fulfill their scientific objective of reaching subatomic-level spatiotemporal resolution. In addition, recently, high-precision timing detection is gaining an unprecedented significance in multi-telescope arrays [10], strain sensing [11], mobile optical clocks [12], time-of-flight detection [13], pulse coherent synthesis [14,15], waveform synthesis [16], soliton characterization [17,18] and many other fields.

Generally, a passively mode-locked solid-state laser exhibits ultra-low timing jitter at high frequencies (e.g., > 100 kHz) [19], which makes it an ideal source for timing detection and characterization. Over the past two decades, several timing detection techniques based on mode-locked lasers have been developed. Initially, timing was directly detected by sending the laser output to a photodetector. This method was severely restricted by the noise introduced by AM-PM conversion [20] (photogenerated carriers, carrier scattering, energy-dependent space charge effects, etc.). To overcome this problem, the balanced optical cross-correlator (BOC) scheme [21,22] was proposed. Due to its simplicity, long-term stability, and immunity to AM-PM noise, it is widely utilized in considerable high-precision timing measurements and applications nowadays [4–7,16–18].

On the other hand, high-precision timing control with low optical power has become imperative in many emerging applications. For example, in ultra-long fiber-based timing link networks, low link operation power can not only reduce the nonlinearity-induced link timing jitter [6], but also enlarge the network's scale with a fixed power budget. Besides, low optical power

#442459 https://doi.org/10.1364/OE.442459
Journal © 2021 Received 6 Sep 2021; revised 10 Oct 2021; accepted 20 Oct 2021; published 1 Nov 2021

Optics EXPRESS

high-precision timing control is also favorable for range measurements on portable devices and quadcopters. However, since the BOC scheme is based on a nonlinear optical effect, it usually cannot provide an adequate timing resolution when the input average optical power is below 1 mW [23] and hence is not suitable for those applications above. Recently, linear-optics timing detection methods based on optical heterodyning have been reported [24,25], which have the potential to work at lower optical power levels, but at the expense of a more complicated setup when compared with a BOC scheme. Therefore, up to now a simple, reliable timing detector operating at low optical power is absent.

To this matter, a new linear-optics-based timing detection scheme is proposed in this work. For our solution, only one acousto-optic modulator (AOM) and a few couplers are required in the optical domain. Using a balanced configuration, the environmental and laser amplitude noise can be well suppressed and attosecond timing precision at 1-mW power level can be achieved. Besides, our detector is intrinsically immune to dispersion effects, so a transform-limited input pulse width is not necessary to guarantee a high timing detection sensitivity.

2. Principle

The principle of the AOM-based timing detector is shown in Fig. 1. The input optical pulse train is launched into an AOM, which diffracts the incident light to different directions. By choosing a proper driving frequency f_{RF} and power for the RF signal, about 50% of the input optical power falls into the 0^{th} and 1^{st} order path, respectively. A time delay element is placed in the 1^{st} order path. After going through this element, some timing error can be imposed on the optical signal. The optical pulse train with a time delay in the 1^{st} order path, and the original pulse train in the 0^{th} order path, are then coupled into a 50:50 fiber coupler and finally beat in a photodetector.

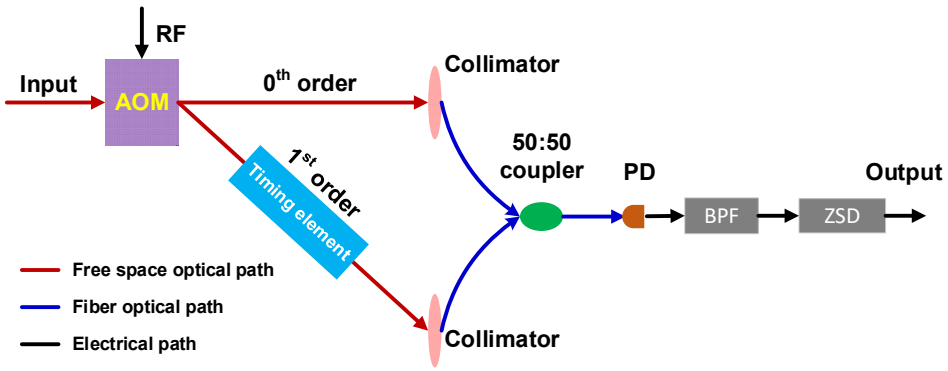

Fig. 1. Principle of the AOM-based linear-optics timing detector. PD, photodetector; BPF, band pass filter; ZSD, zero-bias Schottky diode.

Suppose the electric field of the input optical pulse train is

$$E(t) = \sum_{k=-\infty}^{+\infty} A(t - kT)e^{-j\omega_0 t} \tag{1}$$

where $A(t)$ is the pulse envelope, ω_0 is the angular frequency of the optical carrier, and T is the period of the pulse train. Then at the input ports of the two collimators, the 0^{th} and 1^{st} order diffraction light can be written as

$$E_0(t) = \frac{1}{\sqrt{2}} \sum_{k=-\infty}^{+\infty} A(t - kT)e^{-j\omega_0 t} = \frac{1}{\sqrt{2}} \sum_{n=-\infty}^{+\infty} A_n e^{-j2\pi n f_{rep} t} e^{-j\omega_0 t} \tag{2}$$

Optics EXPRESS

$$E_1(t) = \frac{1}{\sqrt{2}} \sum_{k=-\infty}^{+\infty} A(t - \Delta t - kT) e^{-j(\omega_0+\omega_{RF})(t-\Delta t)} = \frac{1}{\sqrt{2}} \sum_{n=-\infty}^{+\infty} B_n e^{-j2\pi n f_{rep} t} e^{-j(\omega_0+\omega_{RF})(t-\Delta t)} \quad (3)$$

where f_{rep}=1/T is the repetition rate of the pulse train, Δt is the time delay induced by the timing element, A_n and B_n are the Fourier series of the 0th and 1st order pulse train profiles ($B_n = e^{j2\pi n f_{rep}\Delta t} A_n$), and ω_{RF} is the angular frequency of the RF driving signal. After going through the 3-dB coupler, the optical power before the photodetector (PD) is determined by

$$I(t, \Delta t) \propto |E_0 - jE_1|^2 = |E_0|^2 + |E_1|^2 + j(E_0 E_1^* - E_0^* E_1) \quad (4)$$

The band pass filter (BPF) is designed to filter out only the ω_{RF} frequency components. Based on Eq. (2)–(4), the output voltage of the BPF is derived as

$$V_{BPF} \propto j \sum_{n=-\infty}^{+\infty} [A_n B_n^* e^{j[\omega_{RF} t - (\omega_0+\omega_{RF})\Delta t]} - A_n^* B_n e^{-j[\omega_{RF} t - (\omega_0+\omega_{RF})\Delta t]}] \quad (5)$$

Let $X = \left| \sum_{n=-\infty}^{+\infty} A_n B_n^* \right|, j \sum_{n=-\infty}^{+\infty} A_n B_n^* = X e^{j\theta}$, then we have

$$V_{BPF} \propto X \cos[\theta + \omega_{RF} t - (\omega_0 + \omega_{RF})\Delta t] \quad (6)$$

In Eq. (6), the timing information Δt appears in both the amplitude and phase item of V_{BPF}. In our scheme, a zero-bias Schottky diode (ZSD) is used to extract the amplitude of V_{BPF}, so as to make Δt much easier to be resolved. According to the Parseval's theorem, the output of the ZSD satisfies

$$V_{ZSD}(\Delta t) \propto \left| \sum_{n=-\infty}^{+\infty} A_n B_n^* \right|^{\alpha} \propto \left| \int_{-\infty}^{+\infty} A(t) A(t - \Delta t)^* dt \right|^{\alpha} \quad (7)$$

where α is a parameter associated with the nonlinear properties of the Schottky diode, in our experiment, $\alpha \approx 1.382$. For typical pulse shapes (like Gaussian, hyperbolic secant, etc.), there is always an interval of Δt in which V_{ZSD} monotonously changes with Δt. Therefore, the timing information of the timing element can be characterized by Eq. (7).

For example, in Fig. 2, a hyperbolic secant is chosen for the pulse shape. For a pulse width of 170 fs the normalized ZSD output, $V_{ZSD}(\Delta t)/V_{ZSD}(0)$, can be calculated according to Eq. (7). The results for α=1 (red curve) and α=1.382 (blue curve) are shown in Fig. 2(a). Generally, the blue curve corresponds to the direct measurement results after ZSD, while the red curve represents the equivalent timing response at the PD output, which can be used to evaluate the timing noise floor limit of the system. For both of the two curves in Fig. 2(a), the highest slope, which is defined as the normalized sensitivity in this paper, can be obtained when the ZSD output is close to 0.5. At this point, the ZSD output can be approximately regarded as linear with Δt and the AOM detector exhibits the maximum timing sensitivity. From Eq. (7) one can infer that the normalized sensitivity only depends on the pulse shape and pulse width τ. In Fig. 2(b), the calculated normalized sensitivities with different hyperbolic secant pulse widths are given, showing that the shorter the pulse width is, the more sensitive the timing detector becomes.

In general, the timing resolution of the AOM detector is limited by its noise floor, which is mainly contributed by the shot noise and electronic detector noise. Based on Schottky's theorem, the equivalent AM noise spectral density contributed by the shot noise can be written as

$$S^2_{\mathrm{AM,shot}} = \frac{2eR_p P_{in}}{(P_{in} R_p)^2} = \frac{2e}{P_{in} R_p} \quad (8)$$

where e is the electron charge, P_{in} is the average input optical power at the photodiode, and R_p is the responsivity of the photodetector. Therefore, the shot-noise-limited timing jitter spectral

Optics EXPRESS

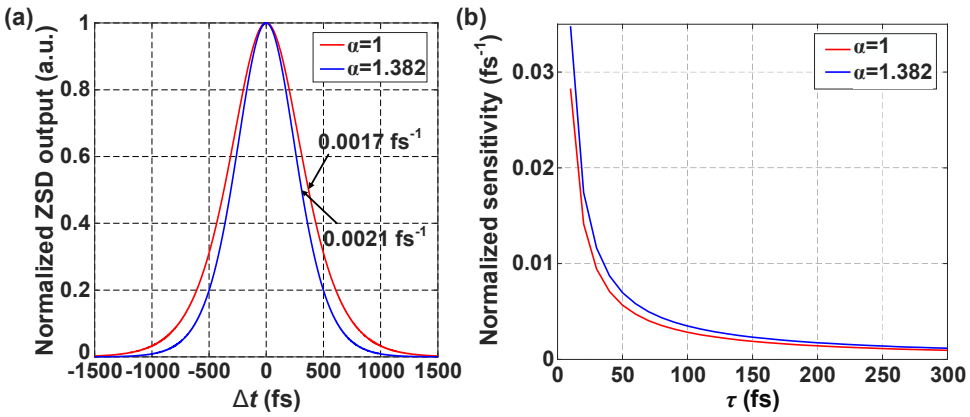

Fig. 2. (a) the relation between Δt and the normalized ZSD output; (b) the relation between the pulse width τ and the normalized sensitivity. For all cases the pulse is hyperbolic secant.

density (TJSD) is determined by

$$S_{T,\text{shot}}^2 = S_{\text{AM,shot}}^2 \left(\frac{1}{\bar{T}_s}\right)^2 = \frac{2e}{P_{in} R_p \bar{T}_s^2} \tag{9}$$

where $\bar{T}_s$ is the normalized timing sensitivity after the photodetector (i.e., the red curve in Fig. 2(b) with α=1).

Similarly, the equivalent AM noise spectral density contributed by the detector's electronic noise is

$$S_{\text{AM,electronic}}^2 = \left(\frac{\text{NEP}}{P_{in}}\right)^2 \tag{10}$$

where NEP is noise equivalent power of the photodetector. Then the electronic noise-limited TJSD can also be obtained:

$$S_{T,\text{electronic}}^2 = S_{\text{AM,electronic}}^2 \left(\frac{1}{\bar{T}_s}\right)^2 = \left(\frac{\text{NEP}}{P_{in}\bar{T}_s}\right)^2 \tag{11}$$

The total TJSD S_T^2 is the sum of these two sources above:

$$S_T^2 = S_{T,\text{shot}}^2 + S_{T,\text{electronic}}^2 \tag{12}$$

Generally, to achieve a lower timing noise floor, higher input power, higher responsivity, lower NEP, or shorter pulse width (higher $\bar{T}_s$) are required. Using typical values for these parameters, S_T^2 is calculated and shown in Fig. 3. In Fig. 3(a), the pulse width τ is set to 170 fs, it can be seen that S_T^2 is more sensitive to NEP at lower input power levels. That is because the electronic noise decreases faster than shot noise as P_{in} increases, thus S_T^2 is dominated by electronic noise at low input power and by shot noise at high input power. In Fig. 3(b), the NEP is fixed to 2 pW/$\sqrt{\text{Hz}}$, at all input power levels, S_T^2 decreases significantly as the pulse width τ becomes shorter. With 10 fs pulse width and 10 mW input power, a timing noise floor of 4.46×10^{-14} fs^2/Hz (note that this is the original physical noise floor, with the help of post digital processing techniques, such as electronic cross-correlation [26,27], the timing noise floor can be further reduced), which is equal to a timing resolution of 211 ys/$\sqrt{\text{Hz}}$ is achieved. This unprecedented high timing resolution indicates that our AOM detector is a very promising device for ultra-precise timing measurements at low input power levels.

Optics EXPRESS

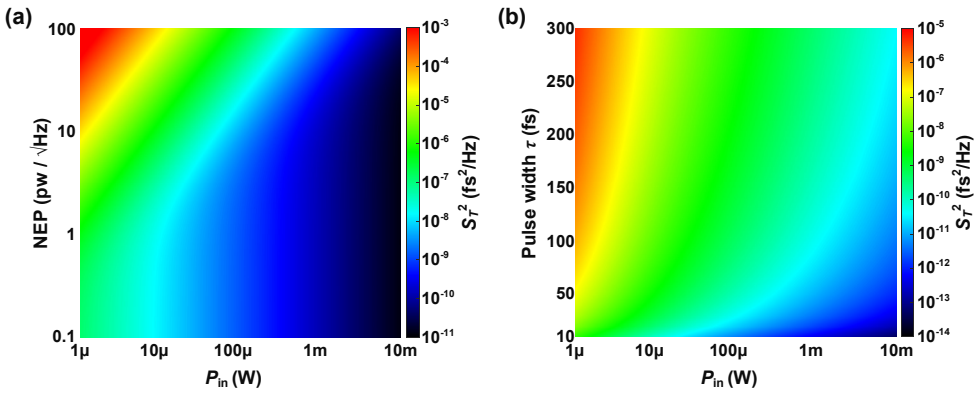

Fig. 3. Timing noise spectral density with (a) different P_{in} and NEP, τ=170 fs and (b) different P_{in} and τ, NEP=2 pW/√Hz. For all cases the pulse is hyperbolic secant and R_p=0.9 A/W.

Based on Eq. (7), if the input optical power fluctuates, the detected voltage V_{ZSD} will also change, which is undesirable for timing error measurement. To solve this problem, we can improve the setup of Fig. 1 using a balanced configuration, as shown in Fig. 4(a). The optical power in the 0th order path is further separated into two branches, with a fixed relative delay of T_D between each other. Then two groups of timing detection between 0th and 1st order pulse trains can be done independently with two PDs, BPFs and ZSDs. After subtraction, the final timing response will become an "s" curve, as shown in Fig. 4(b). Around the zero-crossing point (Δt=0) of the "s" curve, not only the laser's AM noise, but also some common background noise, such as the temperature drift of the whole system, can be canceled. In Fig. 4(b), it can also be seen that the curve with the maximum peak-to-peak voltage (T_D = 800 fs) does not give the maximum slope (timing sensitivity) at Δt=0, therefore, T_D needs to be carefully chosen (close to 500 fs in Fig. 4(b)) to maximize the timing sensitivity around the zero-crossing point.

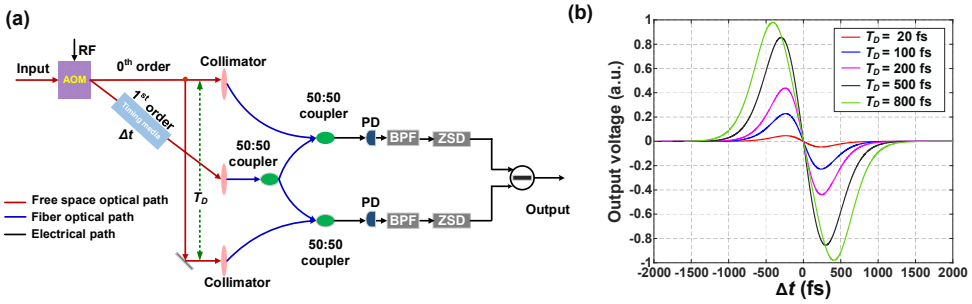

Fig. 4. (a) A balanced scheme of the AOM-based timing detector; (b) The timing characterization curves of the balanced AOM timing detector with different T_D.

Although the background noise can be eliminated by the balanced structure, it should be noted that the noise floor S_T^2 cannot get improved. In fact, because the electronic noise and shot noise generated from the two PDs in Fig. 4(a) are independent, the S_T^2 of balanced detection is twice that of the single detection in Fig. 3. Usually, the balanced structure is helpful in practice since background noise is much higher than S_T^2.

Optics EXPRESS

3. Experimental setup and results

Based on the balanced configuration in Fig. 4(a), an experimental setup to demonstrate the AOM timing detector was built as shown in Fig. 5. The pulse train with 216.667-MHz repetition rate (f_{rep}), 170-fs pulse width and 1555-nm center wavelength generated from a mode-locked laser (MENHIR-1550) is launched into an AOM (Gooch & Housego 3080-197). An 80-MHz RF signal with 200 mV RMS voltage from a function generator is amplified to 3 W to drive the AOM. By carefully adjusting the polarization and incidence angle of the optical input beam, the output power is almost equally separated into the 0th and 1st order diffraction path.

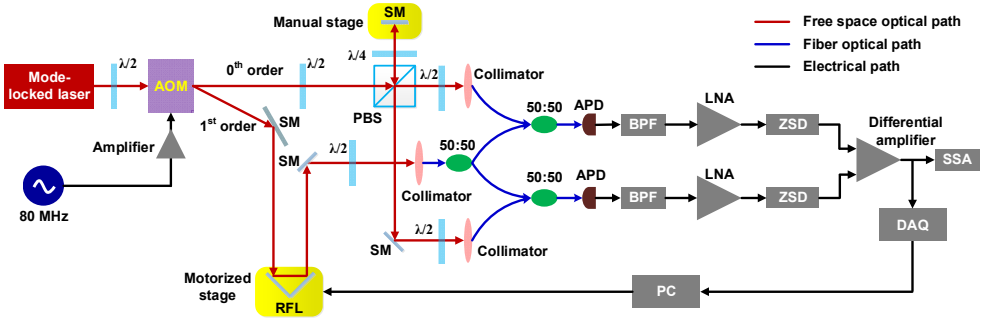

Fig. 5. The experimental setup for the AOM-based linear-optics timing detector. λ/2, half wave plate; λ/4, quarter wave plate; PBS, polarization beam splitter; SM, silver mirror; RFL, retroreflector; 50:50, 3-dB coupler; LNA, low noise amplifier; PC, personal computer.

A motorized stage is placed in the 1st order path to introduce a time delay Δt between the two beams. A manual stage in the 0th order path is used to tune the delay T_D so as to maximize the timing sensitivity in balanced detection. With the help of three 50:50 fiber couplers, the 0th and 1st order pulse trains beat on two avalanche photodiode detectors (APD, CONQUER KG-APR-100M-A-FC). Each APD has a NEP of 2 pW/$\sqrt{\text{Hz}}$, 0.9-A/W responsivity, 50-V/A trans-impedance gain, and 100-MHz 3-dB bandwidth. The 80-MHz beat note from each APD is first filtered out by a BPF and then amplified by a low noise amplifier (LNA, Mini-Circuits ZX60-P103LN+), so as to guarantee that the amplitude fluctuation (i.e., the timing information) of the beat note is high enough to be extracted by a ZSD (Herotek DZR185AA). Finally, the balanced detection is realized by sending the two ZSDs' output to a differential amplifier, of which the 3-dB bandwidth is 1 MHz, and the equivalent input noise voltage density is 0.75 nV/$\sqrt{\text{Hz}}$.

The coupling loss of each collimator is about 3 dB, which can be reduced to <1 dB with customized lenses adapted to the input beam waist. The output signal from the idle ports of the 50:50 couplers can be used to build another AOM timing detector. Therefore, in principle, 80–90% of the input power to the AOM can be efficiently utilized.

To obtain the exact relation between Δt and the ZSD output, i.e., the timing characterization curve, we use a computer to control the motorized stage and collect the output voltage through a data acquisition card (DAQ) simultaneously. Figure 6(a) gives the normalized timing characterization curve of each ZSD (blue and red), the calculation results from Eq. (7) with α=1.382 is also shown (green). A perfect match among these three curves proves the high degree accuracy of our theoretical model. By carefully tuning the manual stage, an s-like curve can be obtained from the differential amplifier output and the timing sensitivity around the zero-crossing point can be maximized. With 1 mW power for each pulse train at each APD (a total input power of 20 mW before the AOM), the timing sensitivity around the zero-crossing is about 43.537 mV/fs (with a measurement error of ±0.0103 mV/fs), as shown in Fig. 6(b). Due to the nonuniformity

Optics EXPRESS

of the two ZSDs, the s-like curve in Fig. 6(b) is a little asymmetric. The AM noise after the two BPFs is measured by a signal source analyzer (SSA) and converted to TJSD at the two APD outputs using the normalized timing sensitivity, as shown in the up of Fig. 6(c) (light blue and light red). The TJSD of the differential amplifier output is also measured by the baseband function of the SSA and shown as the dark blue curve. The differences of the three curves above indicates that the environmental noise and laser's amplitude noise is significantly suppressed by the balanced detection. The minimum measured timing jitter (detection noise floor) after the differential amplifier is about 1×10^{-10} fs^2/Hz, which is close to the shot noise limit (red dashed), estimated by Eq. (9). By choosing PDs with higher responsivity, the detection floor can be further reduced, and it is also possible to approach the standard quantum limit of a pulse train timing jitter predicted by [26] (black dashed), which is only 10 dB lower than the current detection floor.

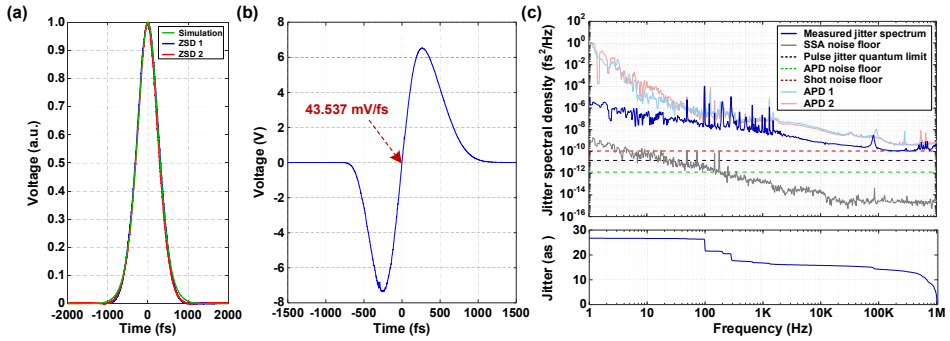

Fig. 6. Measurement results: (a) the normalized timing characterization curve from each ZSD; (b) the timing characterization curve after the differential amplifier; (c) the timing jitter spectral density and corresponding integrated timing jitter.

At the bottom of Fig. 6(c) the integrated timing jitter for balanced detection is also given. The total integrated timing jitter from 1 Hz to 1 MHz is only 26.57 as. The highest noise contribution is from the power line noise at 100 Hz, 200 Hz, 300 Hz, etc. Due to the electrical nonuniformity of the two APDs, each APD exhibits some unique noise that cannot be canceled by the balanced scheme, leading to the bumps around 80 kHz and 500–700 kHz. Using a lower noise power supply, a lower noise RF signal source, and a more similar APD pair, it is possible to further reduce all those technical noise sources. In the absence of those technical noise sources, the residual integrated timing jitter would be about 15 as.

4. Discussions

The AOM-based timing detector has two main inherent merits that make it promising for many applications. First, based on Eq. (7), if the 0th and 1st order pulse trains have the same chirp, the dispersion phase coefficients can be canceled by the product A_nB_n*. Therefore, the input pulses are not required to maintain a transform-limited pulse width to guarantee a high timing detection sensitivity. This feature will be much helpful for the scenarios where the high order dispersion is difficult or expensive to be compensated, but the two pulse trains can easily obtain the same chirp, e.g., a timing sensor based on an ultra-long fiber loop.

Secondly, because the AOM-based timing detector is a linear optical device, it can provide much higher timing resolution at very low power levels compared with nonlinear-optics-based timing detectors, such as BOC. Since a BOC is based on sum frequency generation (SFG), to derive its shot noise and electronic noise-limited timing jitter spectral density, the power P_{in} in Eqs. (9) and (11) should be replaced by the sum frequency generation power $P_{SFG}=\eta_{SFG}P_{in}{}^2$,

Optics EXPRESS

where η_{SFG} is the efficiency of sum frequency generation. Therefore, the total timing noise spectral density of a BOC can be written as

$$S_{BOC}^2 = S_{BOC,\text{shot}}^2 + S_{BOC,\text{electronic}}^2 = \frac{2e}{\eta_{SFG} P_{in}^2 R_p \bar{T}_{BOC}^2} + \left(\frac{NEP}{\eta_{SFG} P_{in}^2 \bar{T}_{BOC}} \right)^2 \tag{13}$$

where $\bar{T}_{BOC}$ is the normalized timing sensitivity of BOC. Based on the study in [28], the photon

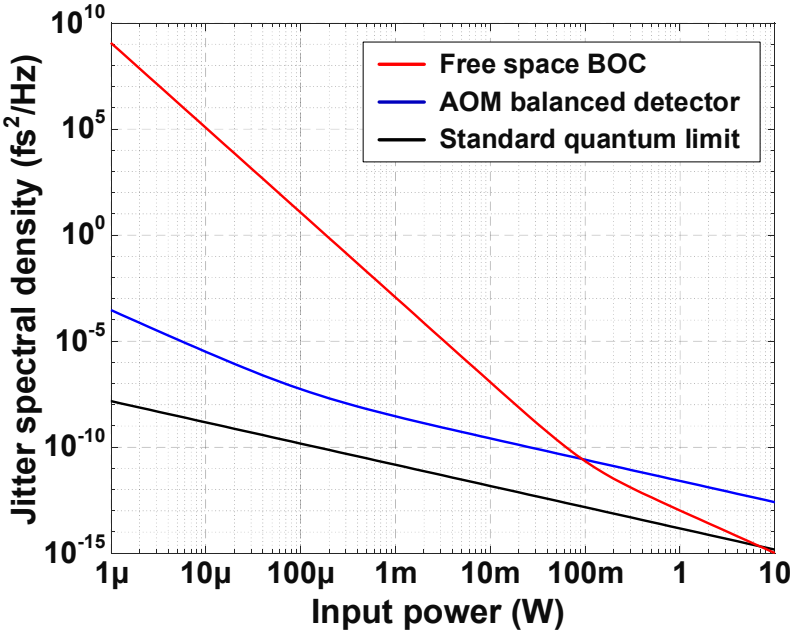

Fig. 7. The timing noise floor of AOM-based balanced detector and BOC at different input average power levels. Pulse width, 170 fs, Nyquist bandwidth, 108.333 MHz; Photodetector responsivity, 0.9 A/W; Photodetector NEP, 2 pW/$\sqrt{\text{Hz}}$; BOC SFG efficiency, $4\times10^{-3}\text{W}^{-1}$.

distribution of optical pulses can lead the standard quantum limit of the timing jitter in a pulse train, which is an additional limiting factor for both the AOM-based timing detector and BOC. The standard quantum limit is determined by the following equation:

$$\left\langle \hat{T}^2 \right\rangle \geq \frac{\tau^2}{N} \tag{14}$$

where $\hat{T}$ is the quantum operator of the pulse temporal center-of-gravity and N is the averaged photon number of each pulse.

In Fig. 7, with 170-fs pulse width, the timing noise spectral density of the AOM-based balanced timing detector and BOC is compared to the standard quantum limit. To make the comparison more objective, the total input power of each detector, which considers the coupling loss in AOM detector and the two polarization components in BOC, is chosen as the x axis of Fig. 7. During the simulation, the input power of the AOM detector is ten times of P_{in} in Eqs. (9) and (11), while the input power of BOC is twice of P_{in} in Eq. (13). For both AOM detector and BOC, the timing noise is dominated by electronic noise at low input power and by shot noise at high input power. Because P_{in} in S_T^2 is replaced by $\eta_{SFG} {P_{in}}^2$ in S_{BOC}^2, as the input power increases, the timing noise of BOC decreases much faster than that of the AOM detector. After about 90 mW,

Optics EXPRESS

BOC outperforms AOM detector and after 7 W, BOC's timing noise floor is even lower than the standard quantum limit, which means BOC is the best timing detector if we do not have any limitations for the input power. On the other hand, for those applications where high input power is not available or the input power has to be restricted for special purposes, the AOM-based timing detector may be a good choice. At very low input power levels, the advantage of the AOM detector is overwhelming. For example, at 1 mW, the timing noise floor of AOM detector is more than 5 orders lower than that of BOC, and at 1 μW this difference even increases to more than 12 orders.

5. Conclusions

In summary, we have proposed an attosecond precision balanced linear-optics timing detection scheme based on AOM. With 1-mW power per pulse train per photodetector, a shot-noise-limited timing detection floor of 1×10^{-10} fs^2/Hz is achieved. Due to the balanced configuration, the environmental and laser amplitude noise is well suppressed. The total integrated jitter from 1 Hz to 1 MHz is only 26.57 as, and the monotone interval in the timing characterization curve is about 500 fs, which is equivalent to 85 dB detection dynamic range. Our timing detector is immune to the same chirp dispersion effects imposed on the two pulses and its timing noise floor is several orders lower than that of BOC when the input power is below 1mW. All the couplers and electronics within the detector can be easily integrated on a chip, which will further improve its robustness and long-term stability. Using some state-of-the-art technology [29], it is also possible to realize a fully-integrated timing detector. With all these merits, we believe that the AOM-based timing detector will be a promising device for many applications, such as high-precision timing link stabilization, remote optical frequency synthesis [30,31], space gravitational wave detection [32] and investigating new timing effects resulting from ultra-low power signals.

Funding. National Key Research and Development Program of China (2019YFB2203600); National Natural Science Foundation of China (61975149).

Disclosures. The authors declare no conflicts of interest.

Data availability. Data underlying the results presented in this paper are not publicly available at this time but may be obtained from the authors upon reasonable request.

References

1. M. Altarelli, R. Brinkmann, M. Chergui, W. Decking, B. Dobson, S. Düsterer, G. Grübel, W. Graeff, H. Graafsma, and J. Hajdu, "XFEL: The European X-Ray Free-Electron Laser," DESY, Technical Design Report (2006).
2. J. Stohr, "Linac Coherent Light Source II (LCLS-II) Conceptual Design Report," SLAC, Design Report, No. SLAC-R-978 (2011).
3. Z. Zhao, D. Wang, Q. Gu, L. Yin, G. Fang, M. Gu, Y. Leng, Q. Zhou, B. Liu, C. Tang, W. Huang, Z. Liu, and H. Jiang, "SXFEL: A Soft X-ray Free Electron Laser in China," Synchrotron Radiation News **30**(6), 29–33 (2017).
4. M. Y. Peng, P. T. Callahan, A. H. Nejadmalayeri, S. Valente, M. Xin, L. Grüner-Nielsen, E. M. Monberg, M. Yan, J. M. Fini, and F. X. Kärtner, "Long-term stable, sub-femtosecond timing distribution via a 1.2-km polarization-maintaining fiber link: approaching 10^{-21} link stability," Opt. Express **21**(17), 19982–19989 (2013).
5. M. Xin, K. Şafak, M. Y. Peng, P. T. Callahan, and F. X. Kärtner, "One-femtosecond, long-term stable remote laser synchronization over a 3.5-km fiber link," Opt. Express **22**(12), 14904–14912 (2014).
6. M. Xin, K. Şafak, M. Y. Peng, A. Kalaydzhyan, W. Wang, O. D. Mücke, and F. X. Kärtner, "Attosecond precision multi-kilometer laser-microwave network," Light: Sci. Appl. **6**(1), e16187 (2017).
7. K. Şafak, M. Xin, M. Y. Peng, and F. X. Kärtner, "Synchronous multi-color laser network with daily sub-femtosecond timing drift," Sci. Rep. **8**(1), 11948 (2018).
8. M. Harmand, R. Coffee, M. R. Bionta, M. Chollet, D. French, D. Zhu, D. M. Fritz, H. T. Lemke, N. Medvedev, B. Ziaja, S. Toleikis, and M. Cammarata, "Achieving few-femtosecond time-sorting at hard X-ray free-electron lasers," Nat. Photonics **7**(3), 215–218 (2013).
9. H. W. Kim, N. A. Vinokurov, I. H. Baek, K. Y. Oang, M. H. Kim, Y. C. Kim, K.-H. Jang, K. Lee, S. H. Park, S. Park, J. Shin, J. Kim, F. Rotermund, S. Cho, T. Feurer, and Y. U. Jeong, "Towards jitter-free ultrafast electron diffraction technology," Nat. Photonics **14**(4), 245–249 (2020).

Optics EXPRESS

10. Y. He, K. G. H. Baldwin, B. J. Orr, R. B. Warrington, M. J. Wouters, A. N. Luiten, P. Mirtschin, T. Tzioumis, C. Phillips, J. Stevens, B. Lennon, S. Munting, G. Aben, T. Newlands, and T. Rayner, "Long-distance telecom-fiber transfer of a radio-frequency reference for radio astronomy," Optica **5**(2), 138–146 (2018).
11. X. Lu, S. Zhang, X. Chen, D. Kwon, C.-G. Jeon, Z. Zhang, J. Kim, and K. Shi, "Ultrasensitive, high-dynamic range and broadband strain sensing by time-of-fight detection with femtosecond-laser frequency combs," Sci. Rep. **7**(1), 13305 (2017).
12. H. Bergeron, L. C. Sinclair, W. C. Swann, I. Khader, K. C. Cossel, M. Cermak, J.-D. Deschênes, and N. R. Newbury, "Femtosecond time synchronization of optical clocks off of a flying quadcopter," Nat Commun **10**(1), 1819 (2019).
13. Y. Na, C.-G. Jeon, C. Ahn, M. Hyun, D. Kwon, J. Shin, and J. Kim, "Ultrafast, sub-nanometre-precision and multifunctional time-of-flight detection," Nat. Photonics **14**(6), 355–360 (2020).
14. G. Mourou, B. Brocklesby, T. Tajima, and J. Limpert, "The future is fibre accelerators," Nat. Photonics **7**(4), 258–261 (2013).
15. R. Betti and O. A. Hurricane, "Inertial-confinement fusion with lasers," Nature Phys. **12**(5), 435–448 (2016).
16. G. M. Rossi, R. E. Mainz, Y. Yang, F. Scheiba, M. A. S. Toledo, S.-H. Chia, P. D. Keathley, S. Fang, O. D. Mücke, C. Manzoni, G. Cerullo, G. Cirmi, and F. X. Kärtner, "Sub-cycle millijoule-level parametric waveform synthesizer for attosecond science," Nat. Photonics **14**(10), 629–635 (2020).
17. Y. Song, F. Zhou, H. Tian, and M. Hu, "Attosecond timing jitter within a temporal soliton molecule," Optica **7**(11), 1531–1534 (2020).
18. C. Bao, M.-G. Suh, B. Shen, K. Şafak, A. Dai, H. Wang, L. Wu, Z. Yuan, Q.-F. Yang, A. B. Matsko, F. X. Kärtner, and K. J. Vahala, "Quantum diffusion of microcavity solitons," Nature Phys. **17**(4), 462–466 (2021).
19. H. A. Haus and A. Mecozzi, "Noise of mode-locked lasers," IEEE J. Quantum Electron. **29**(3), 983–996 (1993).
20. W. Sun, F. Quinlan, T. M. Fortier, J.-D. Deschenes, Y. Fu, S. A. Diddams, and J. C. Campbell, "Broadband Noise Limit in the Photodetection of Ultralow Jitter Optical Pulses," Phys. Rev. Lett. **113**(20), 203901 (2014).
21. T. R. Schibli, J. Kim, O. Kuzucu, J. T. Gopinath, S. N. Tandon, G. S. Petrich, L. A. Kolodziejski, J. G. Fujimoto, E. P. Ippen, and F. X. Kärtner, "Attosecond active synchronization of passively mode-locked lasers by balanced cross correlation," Opt. Lett. **28**(11), 947–949 (2003).
22. F. X. Kärtner, F. Wong, and J. Kim, "Compact background-free balanced cross-correlators," MIT Case 12402, Patent Cooperation Treaty Serial No. US07/085951, Filed November 29, 2007, US Patent 0045974, Filed November 29, 2007, Issued Feb. 25, 2010.
23. M. Xin, K. Şafak, and F. X. Kärtner, "Ultra-precise timing and synchronization for large-scale scientific instruments," Optica **5**(12), 1564–1578 (2018).
24. D. Hou, C.-C. Lee, Z. Yang, and T. R. Schibli, "Timing jitter characterization of mode-locked lasers with <1 zs/$\sqrt{\text{Hz}}$ resolution using a simple optical heterodyne technique," Opt. Lett. **40**(13), 2985–2988 (2015).
25. D. Kwon, C. Jeon, J. Shin, M. Heo, S. E. Park, Y. Song, and J. Kim, "Reference-free, high-resolution measurement method of timing jitter spectra of optical frequency combs," Sci. Rep. **7**(1), 40917 (2017).
26. X. Xie, R. Bouchand, D. Nicolodi, M. Giunta, W. Hänsel, M. Lezius, A. Joshi, S. Datta, C. Alexandre, M. Lours, P.-A. Tremblin, G. Santarelli, R. Holzwarth, and Y. L. Coq, "Photonic microwave signals with zeptosecond-level absolute timing noise," Nat. Photonics **11**(1), 44–47 (2017).
27. A. Casanova, A. Courjaud, B. Trophème, and G. Santarelli, "Measurement of absolute timing jitter of SESAM mode-locked lasers with yoctosecond sensitivity," Opt. Lett. **45**(21), 6098–6101 (2020).
28. V. Giovannetti, S. Lloyd, and L. Maccone, "Quantum enhanced positioning and clock synchronization," Nature **412**(6845), 417–419 (2001).
29. E. A. Kittlaus, W. M. Jones, P. T. Rakich, N. T. Otterstrom, R. E. Muller, and M. R. Zadeh, "Electrically driven acousto-optics and broadband non-reciprocity in silicon photonics," Nat. Photonics **15**(1), 43–52 (2021).
30. M. Xin, N. Li, N. Singh, A. Ruocco, Z. Su, E. S. Magden, J. Notaros, D. Vermeulen, E. P. Ippen, M. R. Watts, and F. X. Kärtner, "Optical frequency synthesizer with an integrated erbium tunable laser," Light: Sci. Appl. **8**(1), 122 (2019).
31. N. Singh, M. Xin, N. Li, D. Vermeulen, A. Ruocco, E. S. Magden, K. Shtyrkova, E. P. Ippen, F. X. Kärtner, and M. R. Watts, "Silicon Photonics Optical Frequency Synthesizer," Laser Photonics Rev. **14**(7), 1900449 (2020).
32. P. A. Seoane, S. Aoudia, S. Babak, P. Binétruy, E. Berti, A. Bohé, C. Caprini, M. Colpi, N. J. Cornish, K. Danzmann, J.-F. Dufaux, J. Gair, O. Jennrich, P. Jetzer, A. Klein, R. N. Lang, A. Lobo, T. Littenberg, S. T. McWilliams, G. Nelemans, A. Petiteau, E. K. Porter, B. F. Schutz, A. Sesana, R. Stebbins, T. Sumner, M. Vallisneri, S. Vitale, M. Volonteri, and H. Ward, "Low-frequency gravitational-wave science with eLISA/NGO," Class. Quantum Grav. **29**(12), 124016 (2012).